systems, for which chaotic dynamics are expected, may spontaneously develop organization under certain conditions[7–9]. Experiments on driven charge-density waves (CDWs) have given strong evidence for the occurrence of such organization[10–12]. Electrical transport measurements on such systems have revealed strong noise for the sliding CDW which, for sufficiently large driving force (the voltage in the case of CDW), develops coherent components at well defined frequencies. The dynamics of CDWs also exhibit various memory effects. The system of weakly pinned vortices is very similar to the pinned CDW state and our findings demonstrate that organization of the dynamics can also occur for the driven vortex lattice. □

Received 29 April; accepted 26 November 1996.

1. Jensen, H. J., Brass, A. & Berlinsky, A. J. *Phys. Rev. Lett.* **60,** 1676–1679 (1988).
2. Yaron, U. *et al. Nature* **376,** 753–755 (1995).
3. Burlachkov, L. *et al. Phys. Rev. B* **50,** 16770–16773 (1994).
4. Gagnon, R., Lupien, C. & Taillefer, L. *Phys. Rev. B* **50,** 3458–3461 (1994).
5. Braun, D. W. *et al. Phys. Rev. Lett.* **76,** 831–834 (1996).
6. D'Anna, G. *et al. Phys. Rev. Lett.* **75,** 3521–3524 (1995).
7. Sarkardei, M. R. & Jacobs, R. L. *Phys. Rev. E* **51,** 1929–1932 (1995).
8. Tang, C., Wiesenfeld, K., Bak, P., Coppersmith, S. & Littlewood, P. *Phys. Rev. Lett.* **58,** 1161–1164 (1987).
9. Coppersmith, S. N. & Littlewood, P. B. *Phys. Rev. B* **36,** 311–317 (1987).
10. Fleming, R. M. & Grimes, C. C. *Phys. Rev. Lett.* **42,** 1423–1426 (1979).
11. Dumas, J., Schlenker, C., Marus, J. & Buder, R. *Phys. Rev. Lett.* **50,** 757–760 (1983).
12. Grüner, G. & Zettl, A. *Phys. Rep.* **119,** 117–232 (1985).

Acknowledgements: S.N.G. is on leave from the Moscow Institute of Radioengineering, Electronics and Automation. We thank H. J. Jensen and A. A. Zhukov for discussions. This work was supported by the UK Engineering and Physical Sciences Research Council. S.N.G. was supported by the Royal Society; L.T. was supported by the Canadian Institute for Advanced Research and the Sloan Foundation.

Correspondence and requests for materials should be addressed to P.A.J.d.G. (e-mail: pajdeg@phys.soton.ac.uk).

Spreading-rate dependence of the extent of mantle melting beneath ocean ridges

Yaoling Niu* & Roger Hékinian†

* *Department of Earth Sciences, The University of Queensland, Brisbane, Queensland 4072, Australia*
† *Department of Marine Geosciences, IFREMER, Centre de Brest, BP37, 29287 Plouzané, France*

Abyssal peridotites and mid-ocean-ridge basalts (MORBs) are complementary products of the mantle melting and melt-extraction processes that create the ocean crust. Studies of abyssal peridotites[1–4] and MORBs[2] have showed that the extent of mantle melting is high beneath hotspot-influenced shallow ridges, and is low beneath deep ridges away from hotspots. These results have led to the recognition of a global correlation of MORB composition with ridge depth[5], and to the notion that mantle temperature variation exerts the primary control on the extent of melting beneath ocean ridges[2,5–8]. This conclusion is, however, based largely on data from slow-spreading ridges in the Atlantic and Indian oceans. At the fast-spreading East Pacific Rise (EPR), there is little correlation between MORB chemistry and ridge depth[9,10], an observation that has proved puzzling[8–12]. Here we show that abyssal peridotites from the EPR[13–21] are extremely depleted in basaltic major-element components—significantly more so than peridotites from ridges away from hotspots in the Atlantic and Indian oceans—indicating that the EPR peridotites are residues of the highest extents of melting. These abyssal peridotite data and existing MORB major-element data[12] both suggest that the extent of mantle melting beneath normal ocean ridges increases with increasing spreading rate.

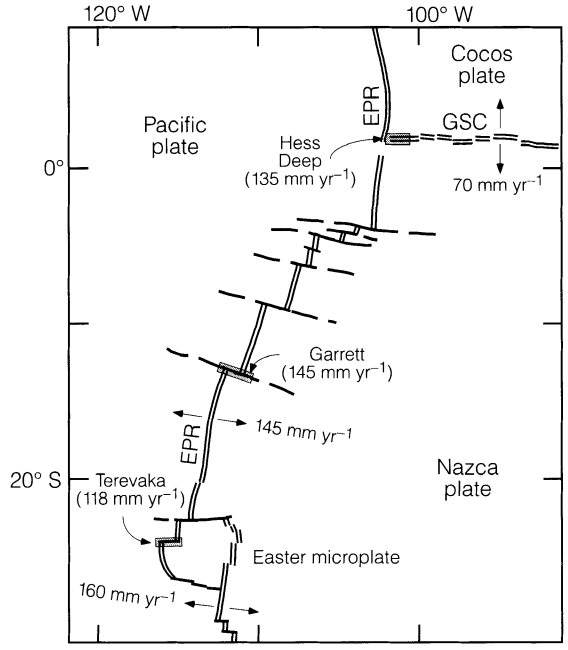

Figure 1 Schematic map of the East Pacific Rise (EPR) axis and the vicinity showing the Hess Deep, Garrett transform and Terevaka transform which are the only locations at the EPR where abyssal peridotites have been recovered[13–21]. GSC is the Galapagos spreading centre. Numbers with mm yr^{-1} are full spreading rates.

There had been no detailed sampling of abyssal peridotites from the EPR until very recent investigations at three localities: Hess Deep[13–15], Garrett transform[16–18] and Terevaka transform[19–21] (Fig. 1). We found that these EPR peridotites are highly depleted harzburgites with little (≤1 vol.%) clinopyroxene, as found in drilled samples at Hess Deep[15]. Residual minerals in these peridotites plot at the most depleted end of the array defined by abyssal peridotite samples from slow-spreading ridges in the Atlantic and Indian oceans (Fig. 2). It has been demonstrated that Cr# (= Cr/[Cr + Al]) in spinel and Al_2O_3 contents in orthopyroxine and clinopyroxene of residual periodotites are sensitive indicators of the extent of melting[1–3,22,23] because Al, a moderately incompatible element during mantle melting, is progressively depleted in these phases during melting. Hence, Fig. 2 shows that the extent of melting beneath the fast-spreading (>110 mm yr^{-1}) EPR is higher than beneath these slow-spreading (≤25 mm yr^{-1}) ridges. Note that this difference in relative extent of melting between fast- and slow-spreading ridges is remarkable when data from hotspot-influenced ridges are excluded. The difference could be ascribed to a less-depleted fertile mantle beneath these slow-spreading ridges than beneath the EPR, but this would be fortuitous.

Although we do not have peridotite data from intermediate-spreading ridges at present, the available data do suggest that the distinct difference in extent of melting may be related to spreading-rate differences. Although abyssal peridotite data are available only from three locations at the EPR, they probably represent the average characteristics of melting residues beneath the EPR, at least in the equatorial and southern region (Fig. 1) because ridges in this broad region, as in other portions of the EPR, have normal depth variation, topography and morphology thermally unaffected by any known hotspots, and erupt MORB that are typical of the EPR[24,25]. Alternatively, the high extents of melting shown by the EPR peridotites could be due to a hotter EPR mantle. However, Zhang and Tanimoto[26] showed that the deeper bound of seismic low-velocity anomalies associated with ocean ridges is ~100 km deep, and is independent of spreading rate. Whereas Su *et al.*[27]

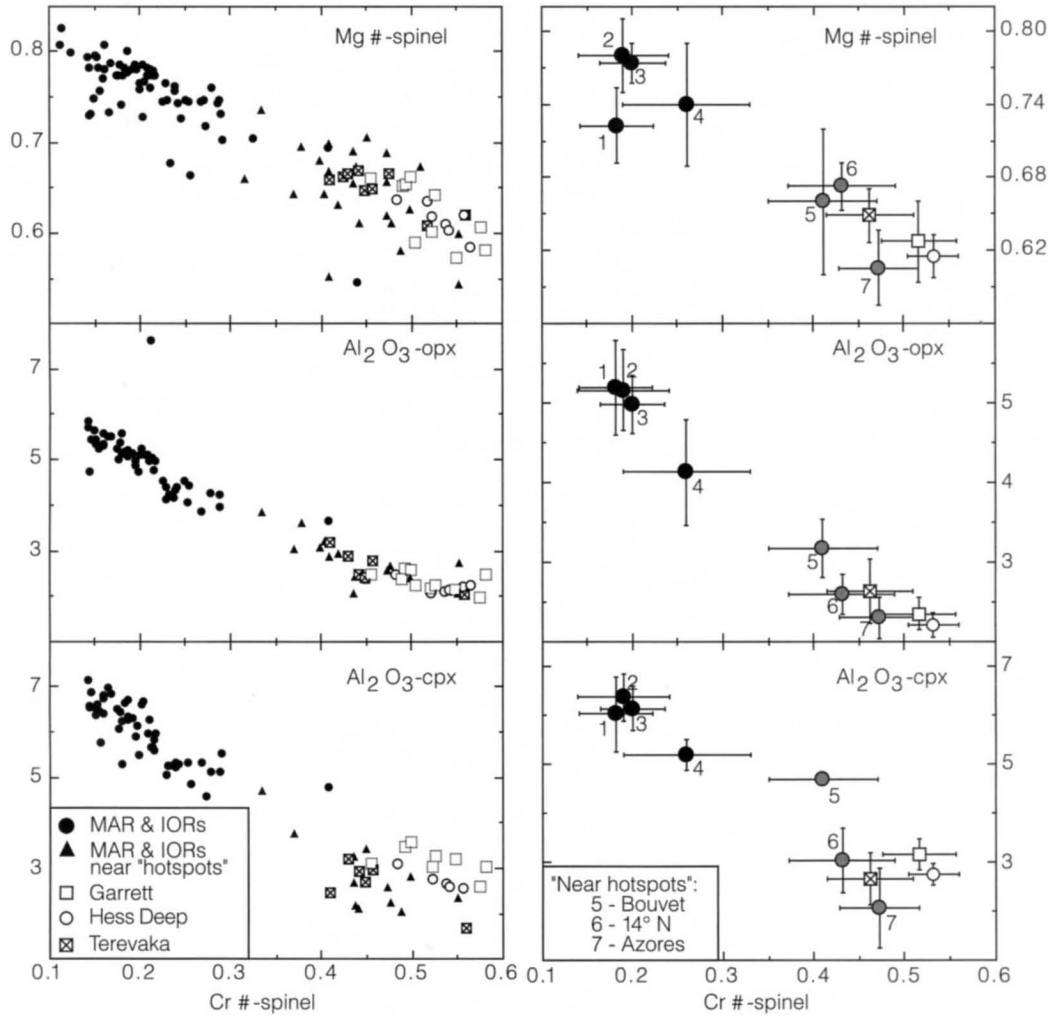

Figure 2 Plots of Cr# (Cr/[Cr + Al]) and Mg# (Mg/[Mg + Fe^{2+}]) in residual spinels and Al_2O_3 contents in residual clinopyroxene (cpx) and orthopyroxene (opx) to show that EPR peridotites plot at the most depleted end of the array defined by samples from slow-spreading ridges in the Atlantic and Indian Oceans. Left panels are the raw data. Right panels are location averages: 1, Atlantis II fracture zone; 2, Vulcan fracture zone; 3, Islas Orcadas fracture zone; 4, Bullard fracture zone; 5, Bouvet fracture zone (near Bouvet hotspot) at the Indian Ocean ridges (IORs); 6, 15° 37′ N axial valley (near 14° N, an incipient mantle plume[42]); and 7, 43° N fracture zone (near the Azores hotspot) at the Mid-Atlantic Ridge (MAR). The data are from refs 1–4, 20, 43–47, and this study. Spreading rates are ≤25 mm yr^{-1} for sample locations in the Atlantic and Indian Oceans (1–7), and ≥110 mm yr^{-1} for sample locations in the Pacific Ocean[48].

argued for a deep (≥300 km beneath all ridges) origin of ocean-ridge seismic-velocity anomalies, work using higher-frequency surface waves suggests[28] that velocity variations beneath ocean ridges are confined to the uppermost 100 km. This suggests that mantle potential temperature variation may not be significant beneath normal ridges unaffected by hotspots[29].

Given the fact that mantle melting beneath ocean ridges is caused by decompression as mantle adiabatically upwells, and that mantle upwelling results from plate separation, fast plate separation at the EPR may be responsible for the high extents of melting evident from the EPR peridotites. If so, it should be evident in MORB chemistry that the extent of mantle melting increases with increasing spreading rate. Indeed, the averaged Al_8 (that is, Al_2O_3 wgt% corrected for crystal fractionation effect to 8.0% MgO; refs 5, 12) and Ca_8/Al_8 in MORB correlate significantly with spreading rate (Fig. 3). Because Al is a moderately incompatible element, its abundance in partial melts decreases while the Ca/Al ratio increases with increasing melting[7,22]. Therefore, correlations in Fig. 3 show that the extent of melting beneath ocean ridges increases with increasing spreading rate. In Fig. 3*a* we plot all the data of ref. 12 averaged within every 15 mm yr^{-1} spreading rate interval. Figure 3*b* shows the data averaged within every 20 mm yr^{-1} interval excluding samples from hotspot-influenced ridges and samples with K/Ti > 0.3 (due to anomalously enriched sources) from all ridges. Apparently, the correlations in Fig. 3*b* are significantly improved when thermal anomalies associated with hotspots and the effect of first-order source compositional variations are removed. Note that the correlations in Fig. 3*b* are better described by curves (power functions) than by straight lines, consistent with model predictions[30,31].

Whereas various differences exist in MORB chemistry between slow- and fast-spreading ridges[7–12,32], previous studies have all concluded that the extent of melting is independent of spreading rate, except at very slow-spreading rates (<20 mm yr^{-1})[29,33], primarily because of the use of Na. There are two apparent difficulties using Na as an indicator of the extent of melting. First, Na is an incompatible minor element, which is known to suffer from fertile mantle heterogeneity[29]. Although abundances of Ca and Al may not be uniform in the mantle, their variability should be relatively small as these elements are major (several per cent) components of mantle material, and their behaviour is largely governed by phase equilibria both under substolidus conditions and during melting[1,22,34]. Second, due to its very incompatible behaviour, Na tends to enter the melt at

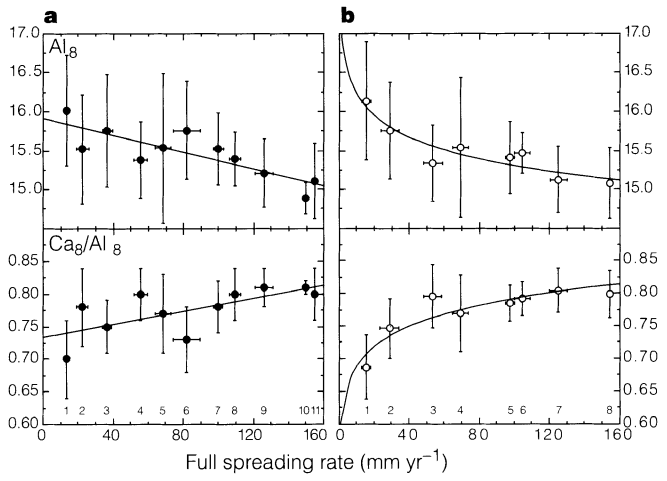

Figure 3 Plots of Al_8 and Ca_8/Al_8 in global MORB averaged by spreading rate against full spreading rate; these statistically significant correlations indicate that the extent of melting increases with increasing spreading rate. The global MORB data base and correction procedure are described in ref. 12. The spreading rate data are from ref. 48. The averaging is done for both spreading rate and Al_8 and Ca_8/Al_8 within a given spreading rate window. The bars are ±1 standard deviation. **a**, All the data averaged within every 15 mm yr^{-1}: 1, spreading rate (SR) <15 mm yr^{-1}, number of samples (N) = 79; 2, SR = 15–30, N = 821; 3, SR = 30–45, N = 204; 4, SR = 45–60, N = 350; 5, SR = 60–75, N = 121; 6, SR = 75–90, N = 17; 7, SR = 90–105, N = 347; 8, SR = 105–120, N = 89; 9, SR = 120–135, N = 6; 10, SR = 135–150, N = 29; 11, SR > 150, N = 239. The correlation coefficients are R = −0.829 for Al_8 and R = 0.685 for Ca_8/Al_8. These R values are significant statistically at >99% and 95% confidence levels respectively. **b**, Data averaged within every 20 mm yr^{-1} after excluding samples from hotspot-influenced ridges/ridge segments (that is, the Iceland, Azores, Galapagos, Juan de Fuca) and samples with K/Ti > 0.3: 1, SR < 20, N = 89; 2, SR = 20–40, N = 431; 3, SR = 40–60, N = 300; 4, SR = 60–80, N = 106; 5, SR = 80–100, N = 176; 6, SR = 100–120, N = 252; 7, SR = 120–140, N = 5; and 8, SR > 140, N = 235. The linear correlation coefficients are R = −0.877 (at <99% confidence levels) for Al_8 and R = 0.791 (at <98% confidence levels) for Ca_8/Al_8. The systematics as a function of spreading rate are, however, better described by simple power functions: $Y = 17.241\,X^{-0.026}$ (R = −0.928) for Al_8 and $Y = 0.579\,X^{0.061}$ (R = 0.912) for Ca_8/Al_8.

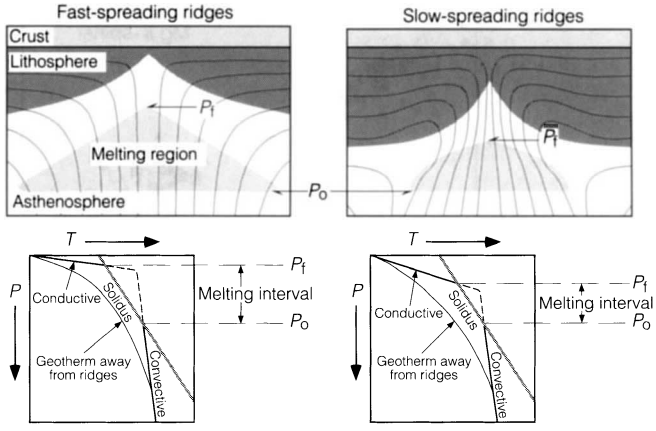

Figure 4 Cartoon comparing uppermost mantle thermal structures between fast- and slow-spreading ridges. Even if the initial melting depth is the same (that is, the same mantle potential temperature), the thermal structure at shallow levels is largely determined by conductive cooling to the surface[30,31,35]. An upwelling mantle along the adiabat (convective thermal gradient) begins to melt when intersecting the solidus at P_0. Decompression melting continues as the melting mantle upwells until conductive cooling to the surface dominates over the adiabat at a shallow level P_f. Fast upwelling beneath fast-spreading ridges allows the adiabat to extend to a shallower level against conductive cooling than slow upwelling beneath slow-spreading ridges. Therefore, below fast-spreading ridges (for example, the EPR), decompression melting continues up to a shallower level, the melting interval between initial (P_o) and final (P_f) depth of melting is larger, and more melt is produced from a given parcel of mantle than beneath slow-spreading ridges (for example, ridges in the Atlantic and Indian oceans). The implication is that the average crust should be thicker in the Pacific than in the Atlantic and Indian oceans. The flowlines are modified from ref. 49.

very early stages of melting. Na abundances in the melt thus decrease rapidly with melting at low extents, but slowly with progressive melting as the result of dilution. Therefore, Na is insensitive to extensive melting, particularly when the effect of source heterogeneity cannot be properly corrected for. In contrast, Ca increases and Al decreases more gradually in the melt with melting. In particular, the Ca/Al ratio increases nearly linearly with increasing melting until clinopyroxene is exhausted at very high extents of melting (≥25%)[7,22]. Therefore, Al and Ca/Al are effective measures of the extent of melting for the entire melting range beneath ridges. The averaged Na_8 is found (data not shown) to exhibit no correlation (such as in Fig. 3*a*) or a weak correlation (such as in Fig. 3*b*; dominated by two points in the <40 mm yr^{-1} range) with spreading rate, which is not surprising given the above reasons. The large variation range (±1 standard deviation) in Al_8 and Ca_8/Al_8 for a given spreading-rate window (Fig. 3*b*) reflects the combined effect of mantle source heterogeneity with respect to these elements, detailed differences in melting processes, and imperfect corrections for crystal fractionation, but the systematics defined by averaged data (averaging out these various factors) as a function of spreading rate is evident.

We propose that the observed variations in extent of melting with spreading rate result from variations in final depth of melting[29] (Fig. 4).

As mantle upwelling beneath ocean ridges results from plate separation, mantle upwelling rate is proportional to spreading rate[30,31,35]. Given the fact that mantle temperature profile beneath a ridge is determined by both convective (adiabat) and conductive thermal gradients[29–31], fast upwelling beneath fast-spreading ridges allows the adiabat to extend to a shallower level against conductive cooling to the surface. By contrast, with slower upwelling beneath slow-spreading ridges, conductive cooling to the surface extends to a greater depth against the adiabat (Fig. 4). Consequently, decompression melting continues up to a shallower level and more melt is produced from a given parcel of mantle beneath fast-spreading ridges than beneath slow-spreading ridges[30,31,36]. Although this concept has long been established[30,36], its effect has not been seriously considered in models[5,6,8] of MORB genesis. Niu and Batiza[7] showed that mantle melting beneath ocean ridges stops at levels significantly deeper than the Moho because MORB chemistry is inconsistent with melting to the Moho. Shen and Forsyth[29] stressed that variation in final depth of melting due to conductive cooling is important in affecting MORB chemistry. Also, Zhang and Tanimoto[26] showed that at a shallow level (for example, at 36 km) beneath ocean ridges, S-wave low-velocity anomalies correlate strongly with spreading rate, indicating a stronger influence of conductive cooling beneath slow-spreading ridges than beneath fast-spreading ridges at this level. Asimow *et al.*[37] argued that the effect of pressure-induced solid–solid phase transitions (that is, garnet–spinel and spinel–plagioclase stability field transitions) is to suppress melting, and may potentially be the cause of melting cessation beneath ocean ridges. Our new observations (Figs 2 and 3), model predictions[30,31,36] and mantle tomographic studies[26], taken together, argue persuasively that the final depth of melting is

primarily determined by the conductive cooling to the surface (Fig. 4). Although a precise determination of the final depth of melting as a function of spreading rate requires more observational data[29], there is the suggestion from ref. 26 that melting may stop at depths ≥30 km beneath very slow-spreading ridges, but at depths perhaps significantly less than 30 km beneath fast-spreading ridges.

Compared with melting residues produced by peridotite melting experiments[22], the highly depleted residual mineral compositions and the extent of depletion to which clinopyroxene is exhausted in the EPR peridotites indicate that these peridotites are residues of ≥25% melting. This high value in extent of melting is significantly higher than 10%, a value that has been advocated to be typical of mantle melting beneath global ocean ridges[38,39]. Calculations[7] show that the range of averaged Al_8 and Ca_8/Al_8 values (Fig. 3) corresponds to ~10% melting at the slow-spreading rate end and ~22% melting at the fast-spreading rate end of the entire spreading rate variation range. Thus, abyssal peridotites and MORB both indicate ≥20% melting beneath the EPR. This suggests that there is no need to invoke long-distance (>60 km) lateral melt migration to the ridge axis required in models that assume 10% melting to explain the crustal accretion at the very narrow axial zone at the EPR (see reviews in refs 31, 35).

Another important implication is that oceanic crust should be, on average, thicker in the Pacific than in the Atlantic and Indian oceans, which is in accord with model predictions that crustal thickness increases with spreading rate[30,31,36]. Although this seems to be inconsistent with the notion (based on seismic velocity data) that oceanic crustal thickness is generally constant (~6–7 km) and is independent of plate spreading rate[33,40], thin crust and peridotite outcrops have been observed within axial zones at slow-spreading ridges[41] but not at fast-spreading ridges. Therefore, crustal thickness derived from seismic data must be used with caution. Relatively few ridges or ridge segments are thermally affected by hotspots. Exclusion of these few anomalies from ridge petrology data sets leads to a clear suggestion that spreading-rate variation is the primary variable that determines both the extent of mantle melting beneath ocean ridges and MORB chemistry. □

Received 25 June; accepted 20 November 1996.

1. Dick, H. J. B. & Fisher, R. L. in *Proc. 3rd Int. Kimberlite Conf* Vol. II (ed. Kompobst, J.) 295–308 (New York, 1984).
2. Dick, H. J. B., Fisher, R. L. & Bryan, W. B. *Earth Planet. Sci. Lett.* **69,** 88–106 (1984).
3. Michael, P. J. & Bonatti, E. *Earth Planet. Sci. Lett.* **73,** 91–104 (1985).
4. Johnson, K. T. M., Dick, H. J. B. & Shimizu, N. *J. Geophys. Res.* **95,** 2661–2678 (1994).
5. Klein, E. M. & Langmuir, C. H. *J. Geophys. Res.* **92,** 8089–8115 (1987).
6. McKenzie, D. & Bickle, M. J. *J. Petrol.* **29,** 625–679 (1988).
7. Niu, Y. & Batiza, R. *J. Geophys. Res.* **96,** 21753–21777 (1991).
8. Langmuir, C. H., Klein, E. M. & Plank, T. in *Mantle Flow and Melt Generation at Mid-ocean Ridges* (eds Phipps Morgan, J., Blackman, D. K. & Sinton, J. M.) 183–280 (AGU Monogr. 71, Am. Geophys Union, Washington DC, 1992).
9. Brodholt, J. P. & Batiza, R. *J. Geophys. Res.* **94,** 4231–4239 (1989).
10. Klein, E. M. & Langmuir, C. H. *J. Geophys. Res.* **94,** 4241–4252 (1989).
11. Batiza, R., Hékinian, R., Bideau, D. & Francheteau, J. *Geophys. Res. Lett.* **22,** 3067–3070 (1995).
12. Niu, Y. & Batiza, R. *J. Geophys. Res.* **98,** 7887–7902 (1993).
13. Francheteau, J. *et al. Earth Planet. Sci. Lett.* **101,** 282–295 (1990).
14. Hékinian, R. *et al. J. Geophys. Res.* **98,** 8069–8094 (1993).
15. Dick, H. J. B. & Natland, J. H. *Proc. ODP Sci. Res.* **147,** 103–134 (1996).
16. Hékinian, R., Bideau, D., Cannat, M., Franchteau, J. & Hébert, R. *Earth Planet. Sci. Lett.* **108,** 259–273 (1992).
17. Hékinian, R., Bideau, D., Herbért, R. & Niu, Y. *J. Geophys. Res.* **100,** 10163–10185 (1995).
18. Constantin, M., Hékinian, R. & Hébert, R. *Geology* (in the press).
19. Francheteau, J. *et al.* (abstr.) *Eos* **75,** 582 (1994).
20. Constantin, M., Hékinian, R., Ackermand, D. & Stoffers, P. in *Mantle and Lower Crust Exposed in Oceanic Ridges and Ophiolites* (eds Visser, R. L. M. & Nicolas, A.) 71–120 (Kluwer, Dordrecht, 1995).
21. Hékinian, R. *et al. J. Volcanol. Geotherm. Res.* (in the press).
22. Jaques, A. L. & Green, D. H. *Contrib. Mineral. Petrol.* **73,** 287–310 (1980).
23. Dick, H. J. B. & Bullen, T. B. *Contrib. Mineral. Petrol.* **86,** 54–76 (1984).
24. Langmuir, C. H., Bender, J. F. & Batiza, R. *Nature* **332,** 422–429 (1986).
25. Sinton, J. M., Smaglik, S. M., Mahoney, J. J. & Macdonald, K. C. *J. Geophys. Res.* **96,** 6133–6155 (1991).
26. Zhang, Y.-S. & Tanimoto, T. *Nature* **355,** 45–49 (1992).
27. Su, W.-J., Woodward, R. L. & Dziewonski, A. M. *Nature* **360,** 149–152 (1992).
28. Phipps Morgan, J., Morgan, J. W., Zhang, Y.-S. & Smith, W. H. F. *J. Geophys. Res.* **100,** 12753–12767 (1995).
29. Shen, Y. & Forsyth, D. W. *J. Geophys. Res.* **100,** 2211–2237 (1995).
30. Reid, I. & Jackson, H. R. *Mar. Geophys. Res.* **5,** 165–172 (1981).
31. Forsyth, D. W. in *Mantle Flow and Melt Generation at Mid-Ocean Ridges* (eds Phipps Morgan, J., Blackman, D. K. & Sinton, J. M.) 1–66 (AGU monogr. 71, Am. Geophys. Union, Washington DC, 1992).
32. Nisbett, E. G. & Pearce, J. A. *Nature* **246,** 468–469 (1973).
33. Bown, J. W. & White, R. S. *Earth Planet. Sci. Lett.* **121,** 435–449 (1994).
34. Dick, H. J. B. *Am. J. Sci.* **277,** 801–832 (1972).
35. Turcotte, D. L. & Phipps Morgan, J. in *Mantle Flow and Melt Generation at Mid-ocean ridges* (eds Phipps Morgan, J., Blackman, D. K. & Sinton, J. M.) 155–182 (AGU monogr. 71, Am. Geophys. Union, Washington DC, 1992).
36. Bottinga, Y. & Allègre, C. *Phil. Trans. R. Soc. Lond. A* **288,** 501–525 (1978).
37. Asimow, P. D., Hirschmann, M. M., Ghiorso, M. S., O'Hara, M. J. & Stolper, E. *Geochim. Cosmochim. Acta* **59,** 4489–4506 (1995).
38. Klein, E. M., Plank, T. & Langmuir, C. H. *RIDGE Events* **2,** 11–12 (1991).
39. Forsyth, D. W. *J. Geophys. Res.* **98,** 16073–16079 (1993).
40. Chen, Y. J. *Geophys. Res. Lett.* **19,** 753–756 (1992).
41. Cannat, M. *J. Geophys. Res.* **101,** 2847–2857 (1996).
42. Bourgault, H. *et al. Earth Planet Sci. Lett.* **88,** 27–36 (1988).
43. Shibata, T. & Thompson, G. *Contrib. Mineral. Petrol.* **93,** 144–159 (1986).
44. Dick, H. J. B. *Geol. Soc. Special Publ.* **42,** 71–105 (1989).
45. Johnson, K. T. M. & Dick, H. J. B. *J. Geophys. Res.* **97,** 9219–9241 (1992).
46. Cannat, M., Bideau, D. & Bougault, H. *Earth Planet. Sci. Lett.* **109,** 87–106 (1992).
47. Hébert, R., Bideau, D. & Hékinian, R. *Earth Planet. Sci. Lett.* **65,** 107–125 (1983).
48. DeMets, C., Gordon, R. G., Argus, D. F. & Stein, S. *Geophys. J. Int.* **101,** 425–478 (1990).
49. Scott, D. R. & Stevenson, D. J. *J. Geophys. Res.* **94,** 2973–2988 (1989).

Acknowledgements: We thank M. Bohn for assistance with mineral microprobe analysis (SX 50 Camebax, IFREMER); and H. Dick and J. Sinton for reviews. The Pacific peridotites were collected during 1990, 1991 and 1993 with the submersible *Nautile* and its support ship *Nadir*. The dives were sponsored by IFREMER and INSU and organized by IFREMER-GM and UBO (Chief Scientists: J. Francheteau for PITO and Hess Deep cruises, and R. Hékinian for Garett cruise). This work was supported by the Bilateral Science and Technology Program of Australia and the Ministère de l'Education de l'enseignement Superior et de la Recherche of France.

Correspondence and requests for materials should be addressed to Y.N. (e-mail: niu@earthsciences.uq.edu.au).

Corrugated slip surfaces formed at ridge–transform intersections on the Mid-Atlantic Ridge

J. R. Cann*, D. K. Blackman*, D. K. Smith†, E. McAllister*, B. Janssen*, S. Mello*, E. Avgerinos*, A. R. Pascoe* & J. Escartin†

* *Department of Earth Sciences, University of Leeds, Leeds LS2 9JT, UK*
† *Woods Hole Oceanographic Institution, Woods Hole, Massachusetts 02543, USA*

The strips of ocean crust formed at the inside corners of both transform and non-transform offsets on the Mid-Atlantic Ridge are punctuated by topographic highs—the 'inside-corner highs'[1–3]—where plutonic rocks (including gabbros and peridotites) are frequently found[4,5]. Current tectonic models consider the inside-corner highs to be lower-crust and upper-mantle materials that have been exhumed by low-angle detachment faults dipping away from the inside corner to beneath the ridge axis[3,6–8]. But much of the evidence for the existence of such faults has hitherto been circumstantial. Here we present sonar images of two ridge–transform intersections on the Mid-Atlantic Ridge (near 30° N), which show that both active and 'fossil' inside-corner highs are capped by planar, dipping surfaces marked by corrugations and striations oriented parallel to the plate spreading direction. Although these surfaces may be the low-angle detachment faults envisaged by the models, they dip at much shallower angles than expected. This could be explained by the lubricating presence of serpentinized peridotite, fragments of which have been dredged from both surfaces. Alternatively, these slip surfaces may instead represent failure surfaces in serpentine-lubricated landslide zones.

Sea-floor morphology in the vicinity of the Atlantis transform fault (Fig. 1) is typical of that near many large transform faults that offset the Mid-Atlantic Ridge. Two strips of anomalous crust ~15 km wide run on either side of the fault trace from the inside corners of the ridge–transform intersections (RTIs) parallel to the